Fully Quantum-State Resolved Study of NO2 Photodissociation: Correlated NO(2.PI..OMEGA., .nu. = 0,J,.LAMBDA.) + O(3Pj) Distributions

3 AUTHORS, INCLUDING:

Andrei Sanov
The University of Arizona
103 PUBLICATIONS **1,452** CITATIONS

Craig R Bieler
Albion College
25 PUBLICATIONS **596** CITATIONS

Fully Quantum-State Resolved Study of NO₂ Photodissociation: Correlated NO(²Π_Ω,v=0,J,Λ) + O(³P_j) Distributions

Andrei Sanov, Craig R. Bieler, and Hanna Reisler*

Department of Chemistry, University of Southern California, Los Angeles, California 90089-0482

Received: March 6, 1995; In Final Form: May 10, 1995[®]

Relative $O(^3P_{j=2,1,0})$ spin−orbit populations correlated with specific $NO[^2\Pi_{\Omega=1/2,3/2}; \nu = 0; J; \Lambda = \Pi(A')$, $\Pi(A'')]$ product states were obtained following photolysis of NO_2 at excess energies $E^\ddagger = 390$, 425, and 1054 cm^{-1}. These fully quantum state-resolved measurements were carried out by recording spatial profiles of recoiling $NO(^2\Pi_\Omega,J,\Lambda)$ products using polarized radiation for photolysis and state-selective laser ionization detection. The relative $O(^3P_j)$ populations correlated with each $NO(^2\Pi_\Omega,J,\Lambda)$ state show marked fluctuations at each excess energy as a function of rotational state and Λ-doublet component. The relative populations also fluctuate as a function of excess energy. The $O(^3P_j)$ spin−orbit population ratios, when averaged over all measurements, exhibit distributions that are colder than statistical, in agreement with previous results. In particular, we find that, on average, $O(^3P_1):O(^3P_2)$ population ratios correlated with the ground $NO(^2\Pi_{1/2})$ state are colder than the corresponding ratios correlated with the excited $NO(^2\Pi_{3/2})$ spin−orbit state. These results are in agreement with the state-specific calculations of Katigiri and Kato [*J. Chem. Phys.* **1993**, *99*, 8805] and are discussed in terms of long-range nonadiabatic transitions among electronic states correlating asymptotically with different spin−orbit states of the ground $NO(^2\Pi) + O(^3P)$ dissociation channel.

I. Introduction

The photodissociation of NO_2 has attracted considerable experimental and theoretical attention. Due to its unique properties, NO_2 has become a model system for testing statistical theories of unimolecular reactions. Usually, in a bond fission reaction proceeding without a barrier, high density of states and intramolecular vibrational redistribution in the excited molecule lead to product state distributions that can be well described by statistical theories, i.e., the product levels are populated as per their degeneracies and quantum state-specific effects are averaged out. In contrast, the unimolecular decomposition of NO_2 represents a case in which both statistical and state-specific dynamical effects are manifest.[1−19]

Due to vibronic chaos at excitation energies >16 000 cm^{-1}, which results from strong couplings between the bright 1^2B_2 state and the ground 1^2A_1 state via a conical intersection,[3,20] the eigenstates in the vicinity of the dissociation threshold ($D_0 = 25\,130.6$ cm^{-1})[1c,14] are strongly mixed and have predominantly 1^2A_1 character.[3a,20,21] Dissociation following $1^2B_2 \leftarrow 1^2A_1$ absorption occurs, therefore, mainly on the ground electronic surface. Despite the extensive state mixing, the vibronic density of states of NO_2 near D_0 is modest (<1 per cm^{-1}).[5,22] Since in addition the number of product channels is relatively small, at least at low excess energies $E^\ddagger$, quantum state-specific effects are expected. Above D_0 the spectrum of NO_2, which remains highly structured, can be described in terms of coherently overlapping resonances.[6,7,23] The state-selected resonance widths gradually increase with $E^\ddagger$,[7] as the dissociation lifetime decreases from a few picosecond just above D_0 to <1 ps at $E^\ddagger \sim 1000$ cm^{-1}.[8,9]

Statistical theories such as Rice−Ramsperger−Kassel−Marcus (RRKM),[24,25] phase-spase theory, (PST)[26,27] or variational RRKM[28,29] prove quite successful in describing the unimolecular reaction rate of NO_2 and the NO rotational and vibrational state distributions, *on average.*[1c,5−8,10,18] At low $E^\ddagger$, the marked fluctuations observed in the product state distribu-

tions were ascribed predominately to quantum interference among overlapping resonances,[6,7,30] but the decomposition of NO_2 appears to be also sensitive to the shape of the potential energy surface (PES) in the transition state (TS) region. For example, the prominent oscillations observed in the NO rotational distributions at higher excess energies (e.g., at $E^\ddagger = 2000-3000$ cm^{-1}) are thought to reflect mappings of bending-like TS wavefunctions onto product rotations.[7,30,31] Likewise, the relative spin−orbit populations in both $O(^3P_j)$ and $NO(^2\Pi_\Omega)$ appear to be colder than statistical[4−6] and apparently depend on the details of the PESs involved and the nonadiabatic couplings among them. Thus, accurate PESs, especially in the region of the TS and beyond, are required for detailed modeling. However, accurate ab initio calculations of surfaces for molecules undergoing barrierless unimolecular reactions are difficult, since in the asymptotic region several electronic states correlating with ground-state products may become important. In addition, the complicated shapes of the wave functions involved in these processes render dynamical calculations even more challenging.

In direct photodissociation processes, dynamical features are often clearly manifest in product state distributions, rates, and absorption spectra, providing many tests for the accuracy of the calculated dissociative PES.[32] This is not the case in barrierless unimolecular reactions. Here, vibrational and rotational distributions are usually well described, on average, by statistical theories, which are inherently rather insensitive to the details of the PES.[33,34] In contrast, the *electronic* degrees of freedom, in particular the product spin−orbit distributions, often deviate substantially from statistical expectations and do not show clear propensity rules, except a tendency to favor channels involving the lowest spin−orbit states of the products.[34] These distributions should depend on those PESs that correlate asymptotically with products in specific spin−orbit states. Describing correctly the behavior of the spin−orbit distributions is important not only for our understanding of nonadiabatic transitions in electronic states but also for calculations of

unimolecular reaction rates, where knowledge of the effective electronic-state degeneracies is required.[35,36]

For NO_2, there are 18 doubly degenerate PESs correlated with $NO(^2\Pi_{1/2,3/2}) + O(^3P_{2,1,0})$.[37] In the asymptotic limit, the splitting between the two spin–orbit states of $NO(^2\Pi)$ is 123 cm^{-1}, while the relative internal energies of $O(^3P_{2,1,0})$ are 0, 158, and 226 cm^{-1}, respectively. Recently, Katagiri and Kato obtained the $NO(^2\Pi_{1/2,3/2}) + O(^3P_{2,1,0})$ PESs near the product region using ab initio calculations including spin–orbit interaction. They also calculated several NO_2 bending–rotation potentials in the region of the TS along the reaction coordinate.[37] The calculations show that only two surfaces are attractive, both correlating with the $NO(^2\Pi_{1/2}) + O(^3P_2)$ channel. Using these potentials, Katagiri and Kato estimated the branching ratios to different $NO(^2\Pi_\Omega) + O(^3P_j)$ spin–orbit channels using a simplified model. When averaged over the NO spin–orbit states, their calculated $O(^3P_{j=2,1,0})$ spin-orbit distributions agree with the experimental results of Miyawaki et al.,[4] and the $NO(^2\Pi_{\Omega=1/2,3/2})$ spin–orbit ratios are also in agreement with experiment.[1,2,6] Furthermore, the state-resolved calculations predict that the $O(^3P_1):O(^3P_2)$ population ratios in the $NO(^2\Pi_{3/2})$ channel should be larger than the corresponding ratios in the $NO(^2\Pi_{1/2})$ channel. It is thus desirable to carry out fully state-resolved measurements in order to test these predictions.

The fully resolved measurements should also provide insight into the issue of fluctuations in state-to-state product distributions and the role of averaging. Marked fluctuations have been observed in the NO *nuclear* degrees of freedom (e.g., in the rotational distributions), which reflect quantum interferences among overlapping resonances;[6,7,30] it is intriguing to see whether the *electronic* degrees of freedom will exhibit fluctuations as well.

In this publication, we describe the use of a simple imaging method to obtain the $O(^3P_j)$ relative spin–orbit population ratios correlated with *single* states of $NO(v,J,\Omega,\Lambda)$. NO_2 is expanded in a molecular beam and photolyzed by a laser polarized in a direction perpendicular to the velocity vector of the molecular beam. The nearly parallel $1^2B_2 \leftarrow 1^2A_1$ transition leads to product recoil predominantly along the laser polarization axis.[11,13,38] After a time delay, the products reach the detection region, which is separated spatially from the photolysis region. Due to their different recoil velocities, $NO(^2\Pi_\Omega,J,\Lambda)$ products correlated with different $O(^3P_j)$ spin–orbit states reach the detection region spatially separated. By scanning the position of the probe laser, the spatial profile of a selected $NO(^2\Pi_\Omega,J,\Lambda)$ product is obtained. The correlation between the $NO(^2\Pi_\Omega,J,\Lambda)$ translational and internal energies is used to generate the relative populations of $O(^3P_{j=2,1,0})$ from the NO spatial recoil profiles. Variants of this approach have been used by other investigators,[13,15,39] but this is the first report of correlated product distributions in the unimolecular reaction of NO_2.

Imaging studies of NO_2 photodissociation were previously carried out using a position sensitive detector,[13] in order to determine the recoil anisotropy parameter β which describes the product angular distribution ($\beta = 2$ and -1 correspond to the limiting cases of a parallel and a perpendicular transition, respectively, and $\beta = 0$ to an isotropic angular distribution).[11–14,40,41] For the in-plane $1^2B_2 \leftarrow 1^2A_1$ transition, the angle between the N–O axis and the transition dipole moment is 23° and the maximum possible value of β is 1.54.[11,13,38] Since the measured value of β depends on parent rotation and dissociation lifetime, it changes with parent rotational temperature and excess energy $E^\ddagger$.[11,13] In supersonic beams, $\beta = 1.2 \pm 0.3$ was found at $T_{rot} = 15$ K and $E^\ddagger = 3038$ cm^{-1}.[13] The recoil anisotropy parameter measured by laser-induced grating

spectroscopy at $E^\ddagger = 126$ cm^{-1} varied in the range $\beta = 0.4-1.5$ depending sensitively on the product recoil velocity (and thus on the NO rotational state).[14]

II. Experimental Section

(a) Experimental Arrangement. The experiments are performed using a differentially pumped, skimmed beam of 2% NO_2 seeded in Ne(70%)/He(30%) carrier gas. The NO_2 mixture is prepared by passing the carrier gas at 2.3 atm pressure over NO_2 kept at -29 °C (*o*-xylene/liquid nitrogen slush). The mixture is expanded through a piezoelectrically actuated pulsed nozzle (0.5 mm aperture, ~150 μs opening time), located ~50 mm away from a 1.23 mm diameter skimmer. The rotational temperature T_{rot} of NO_2 is assumed equal to T_{rot} of background $NO(^2\Pi_{1/2})$ in the molecular beam which is <3 K. The vacuum chamber base pressure is ~2×10^{-7} Torr, and under typical operating conditions (10 Hz nozzle pulse repetition rate) the pressure is <10^{-6} Torr.

A schematic representation of the experimental arrangement is shown in Figure 1. An excimer laser pumped dye-laser system is utilized to excite the expansion-cooled NO_2 into mixed $1^2B_2/1^2A_1$ molecular eigenstates above D_0. The photolysis laser (380–393 nm; 15 ns duration; ~2–4 mJ) is vertically (z) polarized by a Rochon polarizer and intersects the NO_2 beam several centimeters away from the skimmer and ~15 mm before the probe region (see Figure 1). Since the NO_2 transition moment lies in the molecular plane, the product recoil velocities are directed predominantly along the laser polarization (z) axis,[11,38] while the NO + O center of mass (CM) continues to travel with the velocity of the molecular beam, as shown in Figure 2a. The NO product is detected further downstream by a second excimer laser pumped dye laser. Usually, the delay between the photolysis and probe laser pulses is 17.1 μs, while the separation between the two laser beams in the xy plane (see Figure 1) is adjusted to maximize the photodissociation signal. The probe beam (frequency doubled to ~226 nm; 15 ns duration; ~150 μJ) is positioned at the center of the ion detection region defined by the mass-spectrometer extraction plate and acceleration grid (50 mm diameter, 25 mm separation; see Figure 1). The intersection point of the probe laser beam and the z axis is scanned by varying the position of the final prism used in steering the probe beam. In this way, the spatial distributions of the state-selected products are obtained. The step size is typically $\Delta z = 0.15$ mm and the range is $z = -5$ to 5 mm. The pump and probe laser beams are parallel to each other and are at 45° to the molecular beam. The photolysis beam lies in the same horizontal plane (xy) as the NO_2 beam, while the probe beam stays parallel to the xy plane even when scanned along the z axis. To improve the spatial resolution, both the photolysis and probe laser beams are focused with 50 cm focal length lenses; the spot sizes at the center of the chamber are estimated at <0.5 mm.

NO is detected state-selectively by resonant 1+1 multiphoton ionization (REMPI) via the $A^2\Sigma^+ \leftarrow X^2\Pi$ transition using a 1 in. microchannel plate (MCP) detector (Galileo Electro-Optics Corp.) located at the end of a home-built Wiley–McLaren time-of-flight (TOF) mass spectrometer[42] mounted perpendicularly to the xy plane. The recoiling photodissociation products are interrogated within the ion extraction region of the mass spectrometer. Although in this configuration the NO^+ ions arrival time varies slightly with the position of the probe laser beam and the NO product recoil velocity, data acquisition is not affected since the NO^+ signal is collected during a time interval broad enough to cover such variations. A more severe problem arises due to changes in detection sensitivity with the
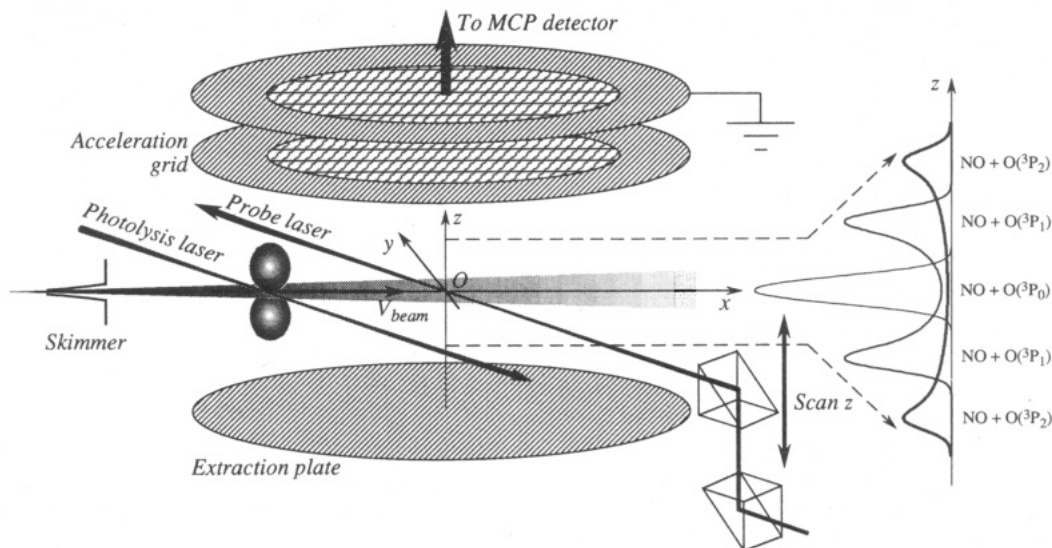
Figure 1. Schematics of the experimental arrangement (not to scale). Shown on the right are examples of the broadened single-mode distributions of NO correlated with different states of $O(^3P_j)$ calculated assuming $^3P_2:^3P_1:^3P_0 = 1:1:0.1$. The $O(^3P_2)$, $O(^3P_1)$, and $O(^3P_0)$ channels have 227, 69, and 1 cm^{-1} available as relative translational energies, respectively. The positions of the NO + $O(^3P_2)$ peaks correspond to $z \approx \pm 4$ mm at a photolysis-probe laser delay of 17.1 μs. A recoil anisotropy parameter $\beta = 1.35$ was used here, as in all other simulated profiles.
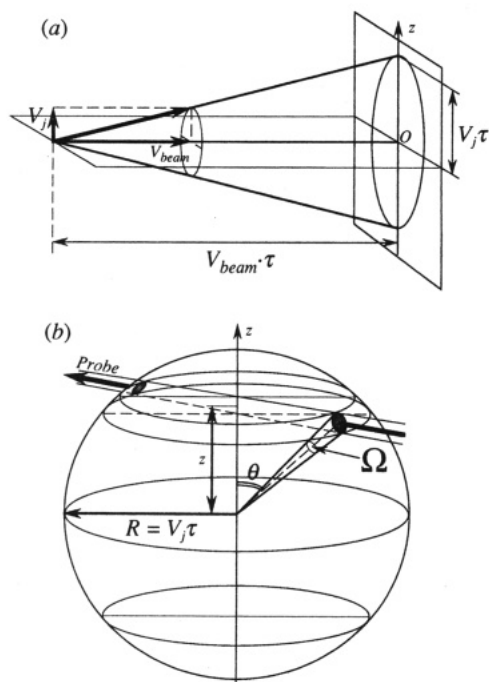

Figure 2. (a) Recoil of products in the laboratory frame. The total NO velocity is the vector sum of the velocity of the NO + O center of mass (equal to the beam travel velocity V_{beam}) and the NO recoil velocity V_j. When the probe laser is fired, NO is at a distance $R = V_j\tau$ from the center of the detection region O, predominantly near the z axis. (b) Sphere of radius $R = V_j\tau$. In the NO + O CM frame the ideal single-channel distribution of NO fragments at a delay τ after photolysis is found on the surface of a sphere of radius $R = V_j\tau$. The NO fragments angular distribution is strongly biased toward the top and the bottom of the sphere, peaking at $\theta = 0$ and π, as discussed in the text. The probe laser beam overlaps two portions of the recoil sphere (shaded areas). If a is the laser beam cross section ($\sqrt{a} \ll R$), each of the two illuminated parts of the sphere has an area $a/\sin \theta$.

probe beam position (z) due to changes in the ion optics focusing conditions. To obtain quantitative information, the observed signal is normalized using a mass spectrometer sensitivity function, which is measured daily by filling the chamber with a small amount of NO ($\sim 10^{-8}-10^{-7}$ Torr partial pressure) and detecting its 300 K isotropic signal as a function of z.

Data acquisition includes shot-to-shot normalization of the

signal using photodiodes to monitor the photolysis and probe pulse energies. The signal is normalized assuming total saturation of the NO $A^2\Sigma^+ \leftarrow X^2\Pi$ transition.[43,44] Although the REMPI intensity is proportional to the number density of the NO molecules, corrections for flux/density transformation are not necessary, since due to the high velocity of the molecular beam the differences in the *laboratory* velocities of the NO products correlated with different $O(^3P_j)$ states are small.

The signal due to background NO in the NO₂ beam was at least 20 times smaller than the NO signal arising from NO₂ photodissociation for the relatively high rotational states of NO probed. At $T_{rot} < 3$ K, only NO in $J < 3.5$ has significant population. Nonetheless, the background signal, having its own spatial (z) distribution due to the spread of the molecular beam, was subtracted on a shot-by-shot basis by operating the photolysis laser in an *on/off* mode. Typically, 150–200 photolysis laser firings were accumulated per data point.

(b) Data Analysis. In describing the simulation of the spatially resolved data, we first consider a case where only one dissociation channel is open (i.e., a single energetically accessible state of $O(^3P_j)$ is correlated with the monitored NO state). This is followed by a discussion of possible spatial broadening factors. The analysis is then extended to simulation of spatial distributions of several channels, including spatial broadening.

Ideal Single-Mode Product Recoil Profile. We follow a classical treatment of the photofragment angular distributions[41] and assume that the NO₂ $1^2B_2 \leftarrow 1^2A_1$ transition dipole moment lies in the molecular plane.[11,38] The NO fragment angular distribution in the NO + O center of mass frame has the form[41]

$$I(\theta) = \frac{\sigma}{4\pi}[1 + \beta P_2(\cos\theta)] = \frac{\sigma}{8\pi}[(2 - \beta) + 3\beta \cos^2 \theta] \quad (1)$$

where σ is the total cross-section, $P_2(\cos \theta) = \frac{1}{2}(3 \cos^2 \theta - 1)$ is the second-order Legendre polynomial, θ is the angle between the laser polarization vector (z axis) and the product recoil direction, and β is the recoil anisotropy parameter. In our simulations we use $\beta = 1.35$ at all three excess energies; this value fits the results when using moderate photolysis laser pulse energies and focusing conditions.

We first consider the product recoil for a single dissociation channel yielding NO + O products in particular quantum states. Without considering the spatial broadening, all the NO fragments

13640 *J. Phys. Chem., Vol. 99, No. 37, 1995*

Sanov et al.

recoil with the same speed V_j, defined in the NO + O CM frame and given by the conservation of energy and momentum:

$$V_j = \sqrt{\frac{2(E^\ddagger - E_{NO} - E_O)}{m_{NO}(1 + m_{NO}/m_O)}} \qquad (2)$$

where E_{NO}, E_O, m_{NO}, m_O are the internal energies and masses of the NO and O fragments. The directions of the recoil velocity vectors in the NO + O CM frame are distributed according to eq 1. At a given time τ after dissociation, all NO fragments lie on a sphere of radius $R = V_j\tau$, as shown in Figure 2b, and their angular distribution, given by eq 1, is biased toward the top and the bottom of the sphere, along the z axis. The probe laser pulse overlaps a portion of this sphere (shaded areas in Figure 2b) when the sphere's center (i.e., the NO + O cm) coincides with the origin of coordinates (O) of the laboratory frame (see Figure 1). At a given z, the observed NO signal is proportional to the product of the angular distribution $I(\theta)$ (eq 1) and the solid angle $\Omega(\theta)$ covered by the probe laser beam (see Figure 2b). If a is the cross section of the laser beam, then in the limit $\sqrt{a} \ll R$ the sphere surface area illuminated by the laser is $2a/\sin\theta$, and the solid angle is $\Omega(\theta) = 2a/(R^2 \sin\theta)$. Substituing $V_j\tau$ for R and $z/(V_j\tau)$ for $\cos\theta$, we obtain the single-mode distribution:

$$w(z; V_j) = N_j\left[(2 - \beta) + 3\beta\frac{z^2}{(V_j\tau)^2}\right]\frac{1}{(V_j\tau)^2\sqrt{1 - \frac{z^2}{(V_j\tau)^2}}} \qquad (3)$$

where N_j is a coefficient proportional to the total number of NO fragments produced in NO_2 photodissociation via the channel under consideration and includes such factors as σ, a, and other instrumental factors, all of which remain constant in the experiment.

Spatial Broadening. The main factors limiting spatial (and thus translational energy) resolution are (i) the finite sizes of the photolysis and probe laser beams, (ii) the z-velocity component of the parent NO_2 molecules in the molecular beam, and (iii) the finite rotational temperature of the parent NO_2 molecules. Thus, the observed profiles are convolutions of function 3 with the spatial broadening function, which we choose

$$g(z) = \exp[-(z/s)^2] \qquad (4)$$

where s is the spatial broadening parameter, whose value, determined in the simulations, is defined by the factors discussed below.

First, the laser beams spot sizes are among the major factors defining the spatial broadening. However, we note that extremely tight focusing conditions are undesirable. Significant saturation of the NO_2 $1^2B_2 \leftarrow 1^2A_1$ transition results in more isotropic distributions of the recoiling products, resulting in a less structured single-mode distribution.

Second, even in a molecular beam, the parent NO_2 molecules have a range of velocities along the z axis. This can be reduced by skimming the molecular beam. Furthermore, the small spot size of the photolysis laser beam acts as a second, smaller (<0.5 mm) skimmer. As a result, the effective *parent* NO_2 velocity spread along the z-axis, compared to the beam travel velocity, is limited by the ratio of the photolysis beam spot size (<0.5 mm) to the skimmer-to-laser beam distance (~50 mm). Thus, the resulting velocity spread along the z axis is less than 1% of the beam travel velocity.
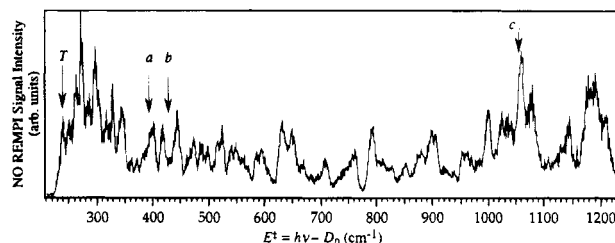

Figure 3. Photofragment yield spectrum of NO_2 obtained by monitoring the $Q_{11} + P_{21}(11.5)$ line of $NO(X^2\Pi_{1/2}(A''),v=0)$ as a function of excess energy. T denotes the $O(^3P_2)$ channel appearance threshold of the monitored NO state; $a{-}c$ indicate excess energies $E^\ddagger = 390$, 425, and 1054 cm^{-1}, respectively, where NO recoil distributions were obtained.

Third, due to the finite rotational temperature of the molecular beam (<3 K) the dissociating NO_2 molecules have a distribution of internal energies, whose width affects the V_z velocity range of products. This effect, however, is small ($\Delta E \sim 3$ K ~ 2 cm^{-1}) and important only within several wavenumbers of the threshold of each particular channel.

In our experiments, the firing delay and the spatial separation between the photolysis and probe laser beams were adjusted to provide adequate signal levels while minimizing spatial broadening. Our observations show that the broadening parameter is nearly constant ($s \sim 0.4$ mm) for photolysis-probe beams delays of 0–20 μs. Therefore, the finite laser beam sizes provide the major source of broadening, as the broadening caused by the parent velocity spread would increase proportionally with the delay. We find that under our experimental conditions longer delays result in improved resolution ($\sim z_{max}/s$).

Multimodal Distributions. The spatial distribution of NO ($^2\Pi_\Omega,J,\Lambda$) in cases when the monitored state of NO is correlated with two (or three) spin−orbit states of $O(^3P_j)$ is given by the sum of two (three) single-mode distributions (eq 3) with different velocity parameters V_j (eq 2), convoluted with the spatial broadening function 4 and weighted by the relative populations N_j of $O(^3P_j)$:

$$W(z) = \sum_{j=2,1,0} N_jw(z;V_j)\, g(z) \qquad (5)$$

The $O(^3P_j)$ spin−orbit ratios are then found from least-squares fits of eq 5 to the experimental data.

The profiles shown on the right-hand side of Figure 1 are examples of broadened single-mode distributions of NO correlated with different states of $O(^3P_j)$. The simulated profiles correspond to a case where the NO + $O(^3P_2)$ channel has 227 cm^{-1} relative translational energy, while 69 and 1 cm^{-1} are available to NO + $O(^3P_1)$ and NO + $O(^3P_0)$ recoil, respectively. The simulation shown is for $^3P_2$:$^3P_1$:$^3P_0 = 1$:1:0.1. The positions of the NO + $O(^3P_2)$ peaks correspond to $z \approx \pm 4$ mm at a photolysis-probe laser delay of 17.1 μs. Note that at $z = 0$ the signal is nonzero for all three single modes; this signal depends on β. Under our experimental conditions ($T_{rot} < 3$ K; $E^\ddagger = 390{-}1054$ cm^{-1}), the simulations are not very sensitive to the exact value of β and its variations for the slowly recoiling products (see section III); the value $\beta = 1.35$ succesfully reproduces our experimental observations.

III. Results

A portion of the NO_2 photofragment yield spectrum obtained by monitoring $NO[^2\Pi_{1/2}(A'');J = 11.5]$ with the photolysis and probe laser beams overlapped is displayed in Figure 3. Arrows $a{-}c$ indicate the three energies $E^\ddagger = 390$, 425, and 1054 cm^{-1}
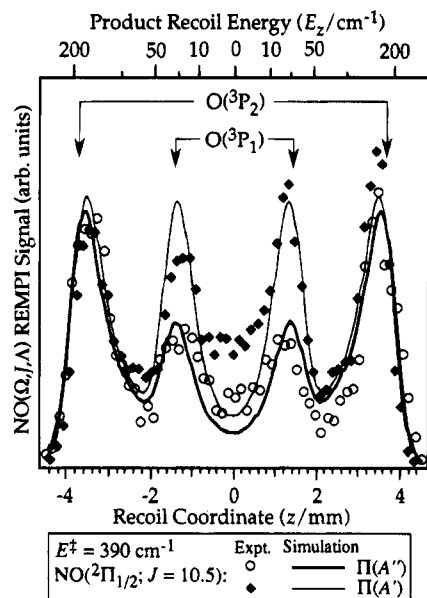
NO₂ Photodissociation

J. Phys. Chem., Vol. 99, No. 37, 1995 **13641**

Figure 4. Spatial profiles of $NO(^2\Pi_{1/2};J = 10.5)$ obtained at $E^{\ddagger} = 390$ cm^{-1} and their least-squares fits. The $R_{21}(10.5)$ line was used to obtain the spatial distribution of NO in the $\Pi(A'')$ Λ-doublet state, while the $R_{11} + Q_{21}(10.5)$ transition was used to detect NO in the $\Pi(A')$ state. The arrows indicate the peaks correlated with the $^3P_2$ and $^3P_1$ spin–orbit states the O atom. The bottom axis represents the distance along the z axis along which the probe laser is scanned (see Figure 1). The top axis indicates the NO + O relative translational energy *along the recoil (z) axis*, i.e., $E_z = \frac{1}{2}\mu V_z^2$, where μ is the reduced mass of NO + O and V_z is the z projection of the product relative recoil velocity. $\beta = 1.35$ is used in all the simulations. See the text for further details.
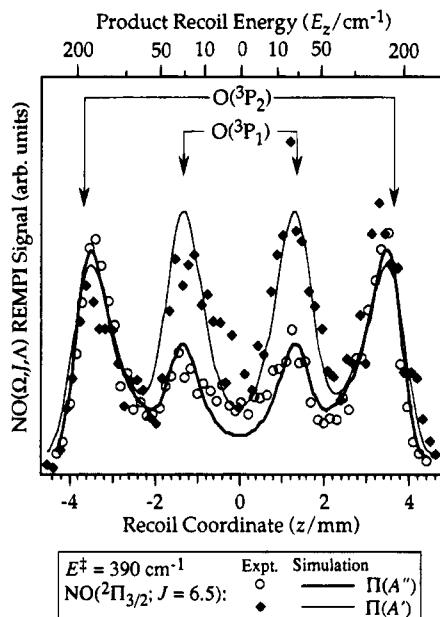

Figure 5. Spatial profiles of $NO(^2\Pi_{3/2};J=6.5)$ obtained at $E^{\ddagger} = 390$ cm^{-1} and their least-squares fits. The $Q_{22} + R_{12}(6.5)$ line was used to obtain the spatial distribution of NO in the $\Pi(A'')$ Λ-doublet state, while the $R_{22}(6.5)$ transition of NO was used to detect NO in the $\Pi(A')$ state. The arrows indicate the peaks correlated with the $^3P_2$ and $^3P_1$ spin–orbit states of the O atom. See Figure 4 for other details.

at which the spatial distributions of the $NO(v=0)$ photofragment in selected quantum states (Ω,J,Λ) were obtained. The excess energies $E^{\ddagger} = 390$ and 425 cm^{-1} were chosen because of the significant fluctuations in the $O(^3P_j)$ population ratio in this energy region previously reported by Miyawaki et al.[4] The higher energy of $E^{\ddagger} = 1054$ cm^{-1} was used to study the evolution of the correlated population ratios as the number of
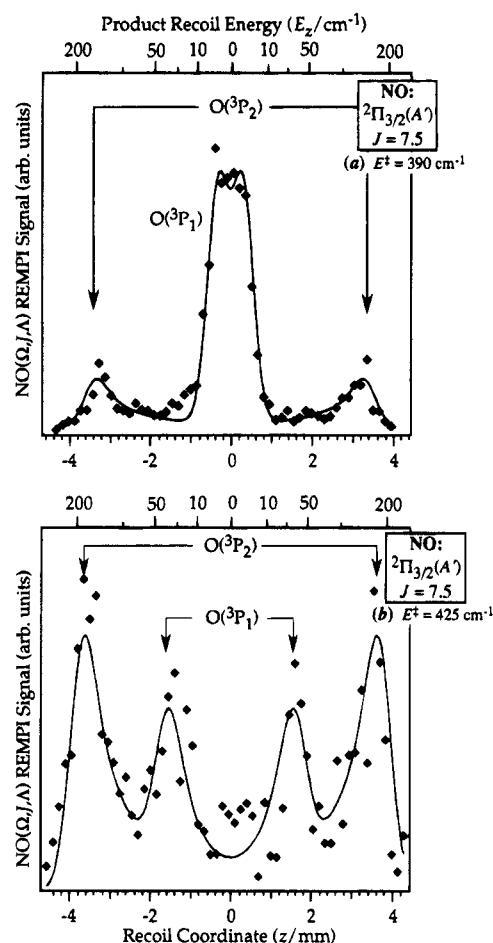

Figure 6. Spatial profiles of $NO(^2\Pi_{3/2};J=6.5;\Pi(A'))$ obtained at (a) $E^{\ddagger} = 390$ cm^{-1} and (b) $E^{\ddagger} = 425$ cm^{-1} by monitoring the $P_{22} + Q_{12}(7.5)$ transition (symbols). The least-squares fits are shown by solid lines. The arrows indicate the peaks correlated with the $^3P_2$ and $^3P_1$ spin–orbit states of the O atom. See Figure 4 for other details.
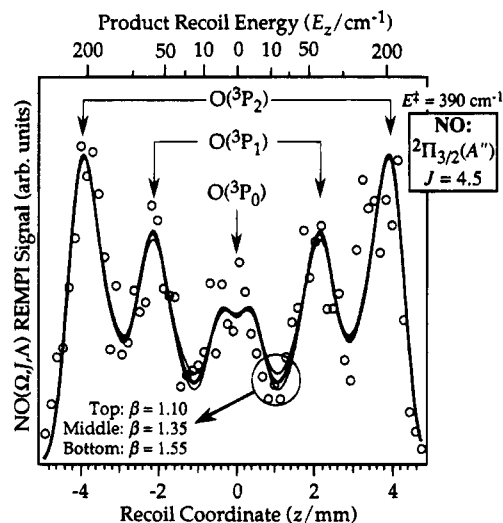

Figure 7. Spatial profile of $NO(^2\Pi_{3/2};J=4.5;\Pi(A''))$ obtained at $E^{\ddagger} = 390$ cm^{-1} by monitoring the $P_{12}(4.5)$ transition (symbols). The arrows indicate the peaks correlated with the $^3P_2$, $^3P_1$, and $^3P_0$ spin–orbit states of the O atom. Shown by the thick line is the least-squares fit with $\beta = 1.35$, while the thin lines show the fits with $\beta = 1.10$ and 1.55. See Figure 4 for other details.

open dissociation channels increases and the dissociation lifetime shortens. As was established earlier, due to the interference among overlapping resonances the exact peak positions in the NO₂ photofragment yield spectrum depend on the monitored
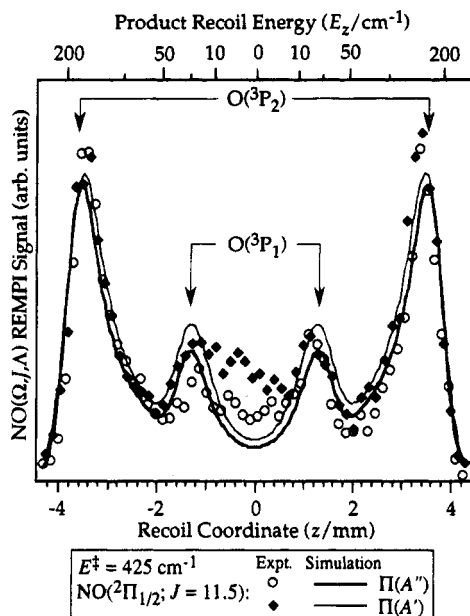
13642 *J. Phys. Chem., Vol. 99, No. 37, 1995*

Sanov et al.

Figure 8. Spatial profiles of $NO(^2\Pi_{1/2};J=11.5)$ obtained at $E^{\ddagger} = 425$ cm^{-1} and their least-squares fits. The $Q_{11} + P_{21}(11.5)$ line was used to obtain the spatial distribution of NO in the $\Pi(A'')$ Λ-doublet state, while the $R_{11} + Q_{21}(11.5)$ transition was used to detect NO in the $\Pi(A')$ state. The arrows indicate the peaks correlated with the $^3P_2$ and $^3P_1$ spin—orbit states of the O atom. See Figure 4 for other details.

Figure 9. Spatial profiles of $NO(^2\Pi_{3/2};J=8.5)$ obtained at $E^{\ddagger} = 425$ cm^{-1} and their least-squares fits. The $Q_{22} + R_{12}(8.5)$ line was used to obtain the spatial distribution of NO in the $\Pi(A'')$ Λ-doublet state, while the $R_{22}(8.5)$ transition was used to detect NO in the $\Pi(A')$ state. The arrows indicate the peaks correlated with the $^3P_2$ and $^3P_1$ spin—orbit states of the O atom. See Figure 4 for other details.
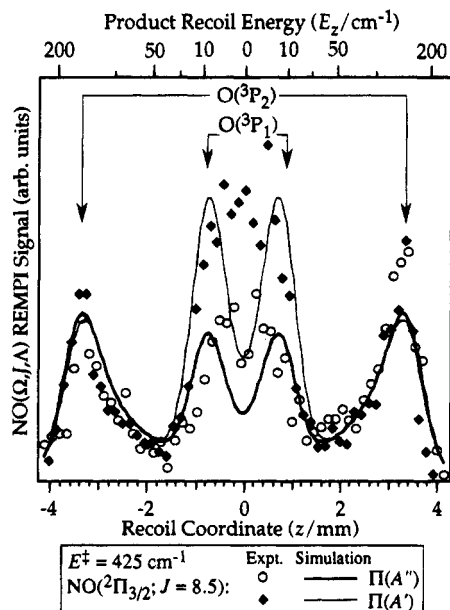
state of NO.[7] Thus, the same excess energy may correspond to a peak maximum for some NO product states and a shoulder for the others. In the reported experiments we chose to keep the selected excess energies constant when monitoring different NO levels.

Representative NO spatial profiles obtained at $E^{\ddagger} = 390$ cm^{-1} are shown in Figures 4, 5, 6(a) and 7. The profiles obtained at $E^{\ddagger} = 425$ cm^{-1} are shown in Figures 6(b), 8, and 9, while those obtained at $E^{\ddagger} = 1054$ cm^{-1} are depicted in Figures 10 and 11. The spatial distributions were obtained at photolysis-probe laser delay of 17.1 μs. The top axis in Figures 4–11 represents the
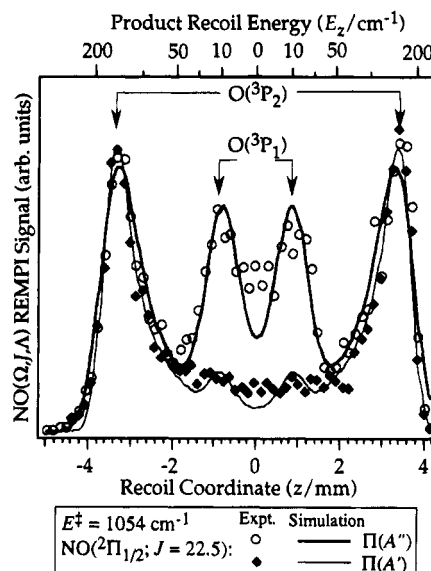

Figure 10. Spatial profiles of $NO(^2\Pi_{1/2};J=22.5)$ obtained in NO_2 photodissociation at $E^{\ddagger} = 1054$ cm^{-1} and their least-squares fits. The $Q_{11} + P_{21}(22.5)$ line was used to obtain the spatial distribution of NO in the $\Pi(A'')$ Λ-doublet state, while the $R_{11} + Q_{21}(22.5)$ transition was used to detect NO in the $\Pi(A')$ state. The arrows indicate the peaks correlated with the $^3P_2$ and $^3P_1$ spin—orbit states of the O atom. See Figure 4 for other details.

NO + O relative translational energy along the recoil (z) axis, $E_z = \frac{1}{2}\mu V_z^2$, where μ is the reduced mass of NO + O, and V_z is the z projection of the product relative recoil velocity.

All the state-selected spatial distributions reveal distinctive peaks correlated with different spin—orbit states of $O(^3P_j)$. As expected, the observed profiles are symmetric with respect to $z = 0$; the symmetric peaks on either side of the center of the detection region correspond to the same product translational energy. Also, monitoring states with similar available translational energies produces similar peak positions in the spatial profiles. For example, profiles generated by monitoring the two Λ-doublet components of each $NO(\Omega,J)$ level have the same peak positions (Figures 4, 5, and 8–10).

The best resolution is achieved for those $NO(^2\Pi_{\Omega},J,\Lambda) + O(^3P_j)$ channels for which the sum of the fragments internal energies is close to the excess energy $E^{\ddagger}$. For example, when the internal energy of the NO + $O(^3P_1)$ channel is close to $E^{\ddagger}$ (e.g., $E^{\ddagger} - E_{NO} - E_O < 100$ cm^{-1}), the translational energy difference between the NO + $O(^3P_2)$ and NO + $O(^3P_1)$ channels ($\Delta E = 158$ cm^{-1}) is larger than the NO + $O(^3P_1)$ channel translational energy, and the peaks correlated with $O(^3P_2)$ and $O(^3P_1)$ are well separated, allowing an accurate determination of the $^3P_1$:$^3P_2$ spin—orbit ratio of oxygen. The $O(^3P_0)$ channel is often not energetically open in such cases. When the $O(^3P_0)$ channel does open, the $O(^3P_0)$ yield is usually quite small [~0.02 of that of $O(^3P_2)$] and difficult to resolve from the signals of the two stronger channels.

For example, Figure 11a depicts the recoil profile of $NO(^2\Pi_{3/2}(A');J=20.5)$ obtained at $E^{\ddagger} = 1054$ cm^{-1}. The two well-separated pairs of peaks correspond to the $O(^3P_2)$ and $O(^3P_1)$ dissociation channels. The product kinetic energies in these channels are 179 and 21 cm^{-1}, respectively. (The product relative translational energies for all studied dissociation channels are listed in Tables 1–3). Figure 11b presents the profile of $NO(^2\Pi_{3/2}(A');J=19.5)$; this channel is 23 cm^{-1} above the appearance threshold of the NO + $O(^3P_0)$ channel. In this case, although all three channels are open, the signal correlated with $O(^3P_0)$ hardly shows up against the $O(^3P_2)$ and $O(^3P_1)$ background because of the small $^3P_0$:$^3P_2$ branching ratio. In contrast,
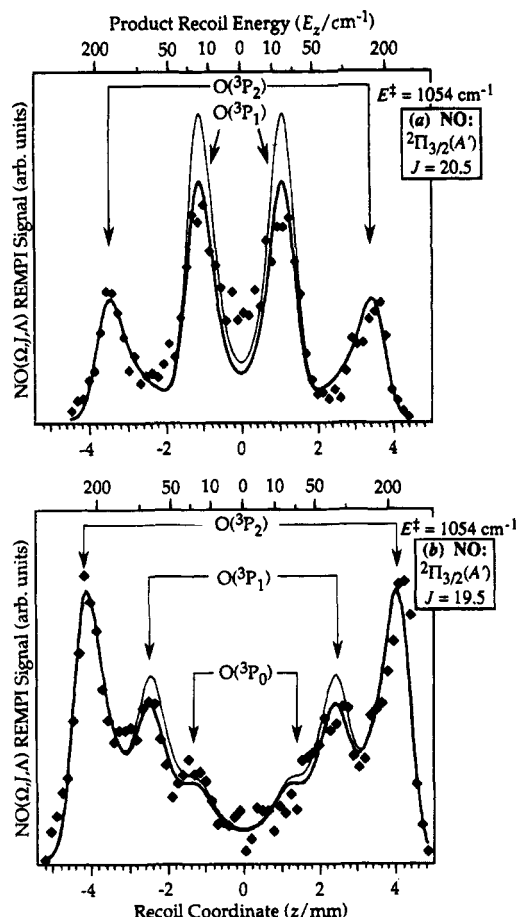
Figure 11. Spatial profiles of (a) $NO(^2\Pi_{3/2};J=20.5;\Pi(A'))$ and (b) $NO(^2\Pi_{3/2};J=19.5;\Pi(A'))$ obtained in NO_2 photodissociation at $E^{\ddagger} = 1054$ cm^{-1} (symbols). The spatial distributions were obtained by monitoring the $P_{22} + Q_{12}(20.5)$ and $P_{22} + Q_{12}(19.5)$ transitions, respectively. The least-squares fits are shown by the thick lines. Shown by the thin lines are the simulations obtained by increasing the $O(^3P_1)$: $O(^3P_2)$ ratio by 30% compared to the values obtained from the least-squares fits. The arrows indicate the peaks correlated with the $^3P_2$, $^3P_1$ and $^3P_0$ spin—orbit states of the O atom. See Figure 4 for other details.

in Figure 7, where $E^{\ddagger} = 390$ cm^{-1} is just 3 cm^{-1} above the appearance threshold of the $NO(^2\Pi_{3/2}(A'');J=4.5) + O(^3P_0)$ channel, the $O(^3P_0)$ peak in the NO spatial distribution is quite intense despite its small relative population. This is due to the small recoil velocity associated with the $O(^3P_0)$ channel and, thus, significant density of the correlated NO. (We note that this effect should not be confused with the conventional flux/density transformation.)

Also shown in Figures 4—11 are the numerical simulations of the observed profiles according to eq 5. Least-square fits to the experimental data, using N_j as a set of adjustable parameters, yield the branching ratios of the $O(^3P_j)$ photofragments correlated with the monitored quantum state of NO. The spin—orbit population ratios obtained in NO_2 photolysis at $E^{\ddagger} = 390$, 425, and 1054 cm^{-1} are listed in Tables 1—3. The error bars reflect the standard deviations of the N_j parameters in eq 5.

In all the simulations, $\beta = 1.35$ was assumed as the recoil anisotropy parameter. Due to the spatial broadening, the result of a simulation is not very sensitive to the value of β. For example, in Figure 7 simulations are shown for three different values, $\beta = 1.10$, 1.35, and 1.55. The difference between the three curves is well within the experimental error bars. The spin—orbit ratios resulting from the fits with different β are also similar: $^3P_2$:$^3P_1$:$^3P_0 = 1:0.22:0.017$, $1:0.24:0.022$, and $1:0.25$: 0.025 for $\beta = 1.10$, 1.35, and 1.55, respectively. In the work

of Houston and co-workers a concern was raised that β might be significantly smaller for the slowly recoiling fragments.[14] However, in our experiment the degree of anisotropy becomes less important when the recoil radius of the products is small and comparable to the probe laser spot-size, since the spatial anisotropy of such recoiling fragments cannot be resolved. It is important, however, that the faster NO fragments correlated with the lower $O(^3P)$ spin—orbit states will have highly anisotropic angular distributions, which will result in better resolved spatial profiles. Thus, the possible poorer degree of anisotropy for the slowly recoiling products would not affect significantly our conclusions.

On the other hand, the simulations are quite sensitive to the $O(^3P_j)$ population ratios. For example, shown by the thick lines in Figure 11a,b are the least-sqaures fits of the experimental profiles. The thin lines represent the simulations of the spatial profiles with the $^3P_1$:$^3P_2$ ratios artificially increased by 30% compared to their least-squares fits values. The differences between the two simulations are well above the error bars. Thus, while not very sensitive to the value of β, the present experimental method is a rather sensitive probe of the $O(^3P_j)$ branching ratios.

The spatial broadening parameter s was individually adjusted for each data set, reflecting slightly different laser focusing conditions. The value of s returned by the least-squares fits was always in the range 0.35—0.5 mm, with most of the data sets clustering close to $s = 0.4$ mm.

As seen from Tables 1—3, at each photolysis energy there are prominent fluctuations in the $O(^3P_j)$ branching ratios correlated with specific final quantum states of NO. In most cases, these fluctuations are clearly visible even without quantitative analysis. In particular, comparisons of the spatial profiles obtained by monitoring different Λ-doublet states within the same rotational level of NO (which differ by only 0.06—0.2 cm^{-1} for $J = 4.5$—22.5) reveal significant differences in the relative intensities of the peaks correlated with $O(^3P_2)$ and $O(^3P_1)$ (see Figure 4, 5, and 8—10). The difference is especially striking in the case depicted in Figure 10 [$E^{\ddagger} = 1054$ cm^{-1}, $NO(^2\Pi_{1/2};J=22.5)$], where the profile of the $\Pi(A'')$ Λ-doublet component shows a pair of prominent peaks correlated with $O(^3P_1)$, while in the $\Pi(A')$ profile the $O(^3P_1)$ peaks can hardly be discerned at the wings of the $O(^3P_2)$ peaks. Quantitatively, the $O(^3P_1)$:$O(^3P_2)$ population ratio in the latter case is 7 times smaller than that correlated with the $\Pi(A'')$ state of NO (see Table 3). Obviously, the observed difference cannot be attributed to the energy difference between the Λ-doublet components (0.06—0.2 cm^{-1}) and must be considered as a quantum state-specific effect.

The fluctuations in the $O(^3P_1)$:$O(^3P_2)$ population ratios with respect to Λ-doublet components do not reveal a consistent bias for any of the Λ-doublet states. For example, in the case discussed above, the $\Pi(A'')$ state correlates with a much warmer $O(^3P)$ spin—orbit distribution than $\Pi(A')$, while the opposite is true in the examples shown in Figures 4, 5, and 9. In the case depicted in Figure 8, the difference does not exceed the error bars. Likewise, comparing the $O(^3P_j)$ branching ratios correlated with different rotational states of NO reveals significant fluctuations at all three excitation energies and for both NO spin—orbit manifolds.

Finally, Figure 6 illustrates the change in the recoil profile of $NO(^2\Pi_{3/2}(A');J=7.5)$ when the excitation energy increases from $E^{\ddagger} = 390$—425 cm^{-1}. At $E^{\ddagger} = 390$ cm^{-1} (Figure 6a) the NO + $O(^3P_1)$ channel has just opened (2 cm^{-1} translational energy) and the corresponding peak is quite significant compared to the NO + $O(^3P_2)$ channel. At $E^{\ddagger} = 425$ cm^{-1} (Figure 6b), more energy is available for recoil of the products in the same

TABLE 1: Products Translational Energies and O(^{3}P) Spin—Orbit Ratios Correlated with Different Quantum States of NO Following NO$_2$ Photolysis at $E^{\ddagger}$ = 390 cm^{-1}

NO quantum state		NO(Ω,J) + O(^{3}P) rel translational energy (cm^{-1})			NO branch probed	O(^{3}P) rel populations				figures
						correlated to NO(Ω,J) Π(A'')		correlated to NO(Ω,J) Π(A')		
Ω	J	O(^{3}P$_2$)	O(^{3}P$_1$)	O(^{3}P$_0$)		O(^{3}P$_1$):O(^{3}P$_2$)	O(^{3}P$_0$):O(^{3}P$_2$)	O(^{3}P$_1$):O(^{3}P$_2$)	O(^{3}P$_0$):O(^{3}P$_2$)	
$2\Pi_{1/2}$	10.5	189	31	—[a]	R$_{21}$, R$_{11}$	0.13 ± 0.01	—	0.25 ± 0.02	—	4
	9.5	224	66	—	R$_{21}$	0.17 ± 0.02	—	N/A[b]	—	
	8.5	256	98	30	Q$_{11}$, R$_{11}$	0.20 ± 0.01	0.044 ± 0.006	0.13 ± 0.02	<0.7	
$2\Pi_{3/2}$	7.5	160	2	—	P$_{22}$	N/A	—	0.31 ± 0.03	—	6a
	6.5	188	30	—	Q$_{22}$, R$_{22}$	0.13 ± 0.01	—	0.34 ± 0.02	—	5
	5.5	210	52	—	R$_{22}$	N/A	—	0.08 ± 0.01	—	
	4.5	229	71	3	P$_{12}$	0.24 ± 0.02	0.022 ± 0.003	N/A	N/A	7

[a] In Tables 1—3, — means the channel is not energetically accessible. [b] N/A indicates that the experimental data for this particular channel are not available due to experimental difficulties.

TABLE 2: Products Translational Energies and O(^{3}P) Spin—Orbit Ratios Correlated with Different Quantum States of NO following NO$_2$ Photolysis at $E^{\ddagger}$ = 425 cm^{-1} [a]

NO quantum state		NO(Ω,J) + O(^{3}P) rel translational energy (cm^{-1})			NO branch probed	O(^{3}P) rel populations				figure
						correlated to NO(Ω,J) Π(A'')		correlated to NO(Ω,J) Π(A')		
Ω	J	O(^{3}P$_2$)	O(^{3}P$_1$)	O(^{3}P$_0$)		O(^{3}P$_1$):O(^{3}P$_2$)	O(^{3}P$_0$):O(^{3}P$_2$)	O(^{3}P$_1$):O(^{3}P$_2$)	O(^{3}P$_0$):O(^{3}P$_2$)	
$2\Pi_{1/2}$	11.5	186	28	—	Q$_{11}$, R$_{11}$	0.09 ± 0.01	—	0.11 ± 0.01	—	8
$2\Pi_{3/2}$	8.5	168	10	—	Q$_{22}$, R$_{22}$	0.12 ± 0.02	—	0.27 ± 0.03	—	9
	7.5	195	37	—	P$_{22}$	N/A	—	0.19 ± 0.02	—	6b

[a] See footnotes to Table 1.

TABLE 3: Products Translational Energies and O(^{3}P) Spin—Orbit Ratios Correlated with Different Quantum States of NO following NO$_2$ Photolysis at $E^{\ddagger}$ = 1054 cm^{-1} [a]

NO quantum state		NO(Ω,J) + O(^{3}P) rel translational energy (cm^{-1})			NO branch probed	O(^{3}P) rel populations				figure
						correlated to NO(Ω,J) Π(A'')		correlated to NO(Ω,J) Π(A')		
Ω	J	O(^{3}P$_2$)	O(^{3}P$_1$)	O(^{3}P$_0$)		O(^{3}P$_1$):O(^{3}P$_2$)	O(^{3}P$_0$):O(^{3}P$_2$)	O(^{3}P$_1$):O(^{3}P$_2$)	O(^{3}P$_0$):O(^{3}P$_2$)	
$2\Pi_{1/2}$	22.5	171	13	—	Q$_{11}$, R$_{11}$	0.14 ± 0.01	—	0.022 ± 0.003	—	10
	21.5	246	88	20	R$_{21}$	0.11 ± 0.01	0.017 ± 0.005	N/A	N/A	
$2\Pi_{3/2}$	20.5	179	21	—	P$_{22}$	N/A	—	0.44 ± 0.03	—	11a
	19.5	249	91	23	P$_{22}$	N/A	N/A	0.18 ± 0.01	0.022 ± 0.005	11b

[a] See footnotes to Table 1.

channel. Nevertheless, the ^{3}P$_1$:^{3}P$_2$ population ratio decreases by more than a third (see Tables 1 and 2). This example provides evidence that the O(^{3}P) spin—orbit ratios fluctuate with the excess energy when monitoring the same fully resolved dissociation channel.

IV. Discussion

The statistical branching ratio of O(^{3}P$_j$) correlated with any *single* quantum state of NO is ^{3}P$_2$:^{3}P$_1$:^{3}P$_0$ = 1:0.6:0.2 as dictated by the degeneracies; when only the O(^{3}P$_{2,1}$) channels are accessible, their statistical ratio is = 1:0.6. In contrast, when the O(^{3}P$_j$) product is detected unresolved with respect to the correlated states of NO, as is usually the case, the observed relative populations of O(^{3}P$_j$) are the sums of the O(^{3}P$_j$) yields correlated with all allowed states of the counterpart NO fragment. Under these circumstances, the statistical O(^{3}P$_j$) branching ratio is obtained by counting all open NO($^2\Pi_\Omega$,v,J,Λ) + O(^{3}P$_j$) channels, and the ^{3}P$_2$:^{3}P$_1$:^{3}P$_0$ population ratios increase gradually with $E^{\ddagger}$. The experiments by Miyawaki et al. show significant deviations from statistical expectations, although the above population ratios increase with $E^{\ddagger}$ at low energies.[4] The average O(^{3}P$_j$) branching ratio is much colder than statistical and at higher excess energies approaches an asymptotic value of ^{3}P$_2$: ^{3}P$_1$: ^{3}P$_0$ = 1:0.19:0.03. Both ^{3}P$_1$:^{3}P$_2$ and ^{3}P$_0$:^{3}P$_2$ spin—orbit ratios reveal oscillatory dependence on $E^{\ddagger}$.[4] These oscillations, which can reach a 5-fold change within a ~10 cm^{-1} interval (e.g., near $E^{\ddagger}$ ~ 400 cm^{-1}), diminish considerably as the excess energy increases.

Our experiments remove the averaging over the accompanying NO product's quantum states and thus yield the branching ratios for the fully resolved dissociation channels. We point out, however, that since in our experiments the best resolution is achieved when the product translational energy is low, we detect mainly high NO(J) states with relative translational energy of 10—250 cm^{-1}. Our results show that fluctuations in the O(^{3}P$_j$) branching ratios occur not just as a function of excess energy, but on a more fundamental level, i.e., with respect to the fully resolved quantum state of the correlated NO fragment. These fluctuations do not appear to diminish with $E^{\ddagger}$. For example, at $E^{\ddagger}$ = 1054 cm^{-1} we observe a marked difference in the ^{3}P$_1$:^{3}P$_2$ ratios when monitoring the channels correlated with the same NO($^2\Pi_{1/2}$;J=22.5) level but with different Λ-doublet components. These fluctuations may be another manifestation of quantum interference among NO$_2$ overlapping resonances and/or reflect fluctuations in the state-to-state matrix elements that couple, at long range, electronic states which correlate asymptotically with different spin—orbit channels.[6,7,22] In contrast, in the study by Miyawaki et al.,[4] the observed O(^{3}P$_j$) signal is the result of averaging of all the different NO channels. Thus, the fluctuations are partially averaged out, and since the number of open final channels increases with $E^{\ddagger}$, the fluctuations gradually diminish.

In contrast to the O(^{3}P$_j$) results, no strong variations in the NO product spin-orbit ratios with $E^{\ddagger}$ are obtained when the NO($^2\Pi_{1/2,3/2}$,J) populations are summed over all product rotational levels at each $E^{\ddagger}$, although the rotational distributions themselves reveal prominent state-to-state fluctuations and oscillations.[6] At excess energies comparable to those used in the present experiments, the separate rotational distributions of NO($^2\Pi_{1/2}$,Λ) and NO($^2\Pi_{3/2}$,Λ) reveal random fluctuations that

diminish upon averaging over the Λ-doublet and spin-orbit states. In contrast, at higher $E^{\ddagger}$ (e.g., $E^{\ddagger} > 2000$ cm^{-1}), the rotation-specific $NO(^2\Pi_{3/2},N):NO(^2\Pi_{1/2},N)$ population ratios ($N = J - \frac{1}{2}$ and $J - \frac{3}{2}$ for $^2\Pi_{1/2}$ and $^2\Pi_{3/2}$, respectively), each being a sum over the two Λ-doublet and three $O(^3P)$ channels, do not change much with $E^{\ddagger}$, and the rotational distributions obtained for each $NO(^2\Pi_{\Omega})$ state show similar oscillatory patterns. In the region $E^{\ddagger} = 2000-3000$ cm^{-1}, $NO(^2\Pi_{3/2}):NO-(^2\Pi_{1/2}) \sim 1:3$.[6] These results suggest that the spin-orbit populations are determined only at long-range, after the rotational distributions have been fixed.[6,7]

Although it is impossible to calculate accurate averages of the $O(^3P_j)$ ratios correlated with different states of NO at each $E^{\ddagger}$, considering the limited number of channels studied, some qualitative conclusions can be drawn. We notice that all the observed spin-orbit distributions of $O(^3P_j)$ are colder than statistical at the excitation energies used. The averages of the $^3P_1:^3P_2$ population ratios are 0.20, 0.16 and 0.18 at $E^{\ddagger} = 390$, 425, and 1054 cm^{-1}, respectively; these values correspond to 33%, 27%, and 30% of the statistical value (0.6). The corresponding averages of the $^3P_0:^3P_2$ population ratios are 0.033 and 0.020 at $E^{\ddagger} = 390$ and 1054 cm^{-1}, respectively; which correspond to 17% and 10% of the statistical value (0.2). On average, these numbers agree well with the results of Miyawaki et al., who estimated the average relative yields of $O(^3P_1)$ and $O(^3P_0)$ at 32% and 15% of statistical, respectively.[4]

An intriguing observation is that despite the fluctuations, the observed $O(^3P_1):O(^3P_2)$ population ratios correlated with $NO(^2\Pi_{3/2})$ are on average larger than those correlated with the ground spin-orbit state, $NO(^2\Pi_{1/2})$ (see Tables 1-3). At $E^{\ddagger} = 390$, 425, and 1054 cm^{-1} the population ratios, averaged over all available observations, are 0.18, 0.10, and 0.09, respectively, for the $NO(^2\Pi_{1/2})$ channel, and 0.22, 0.19, and 0.31 for the $NO(^2\Pi_{3/2})$ channel. For the related $OH(^2\Pi) + O(^3P)$ system, Graff and Wagner have shown that in the H + O₂ reaction at low energies an adiabatic capture model results in smaller reaction cross sections for the excited fine-structure surfaces,[45] since those surfaces are less attractive than the ground surface. Similarly, in the ab initio calculations for NO₂, Katagiri and Kato showed that of the 18 doubly degenerate O−NO electronic surfaces correlated with all the $NO(^2\Pi_{\Omega}) + O(^3P_j)$ products, only two are attractive, both correlating with the $NO(^2\Pi_{1/2}) + O(^3P_2)$ asymptotic limit; all other PESs are repulsive, as shown in Figure 12.[37] Thus, the splitting between each of the two attractive surfaces correlating with $NO(^2\Pi_{1/2}) + O(^3P_2)$ and any other surface is probably larger at shorter O−NO separations than the splitting between any other two surfaces. This implies that the probability for nonadiabatic transitions from the attractive surfaces to any of the excited fine-structure surfaces becomes rather small at shorter O−NO separations. Since only the $NO(^2\Pi_{1/2}) + O(^3P_2)$ asymptotic limit correlates with the attractive surfaces and the lowest of these surfaces correlates with the ground electronic state of NO₂ on which the reaction proceeds, it is not surprising that cold spin-orbit populations are obtained. On the other hand, all the surfaces correlating with $NO(^2\Pi_{3/2})$ are repulsive, and thus nonadiabatic transitions between these surfaces are more likely, explaining the propensity for larger $O(^3P_1):O(^3P_2)$ population ratios correlated with $NO(^2\Pi_{3/2})$ than with $NO(^2\Pi_{1/2})$.

Katagiri and Kato estimated the branching ratios for different $NO(^2\Pi_{\Omega}) + O(^3P_j)$ spin-orbit channels produced in the dissociation using a simplified model based on the infinite order sudden approximation and the Franck−Condon approximation.[37] The calculated average $O(^3P_j)$ and $NO(^2\Pi_{\Omega})$ population ratios are in good agreement with the experimental results.[4,6] Our
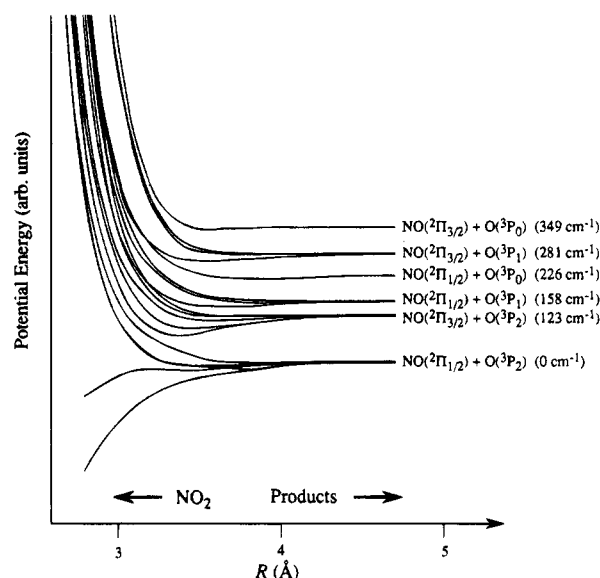

Figure 12. Schematic representation of the 18 doubly degenerate $NO(^2\Pi_{\Omega}) + O(^3P_j)$ adiabatic potential energy curves, adapted from Katagiri and Kato.[37] R is the distance between the receding O atom and the center of mass of NO.

results show that their *state-resolved* values for the $O(^3P_1):O(^3P_2)$ population ratios correlated with the $NO(^2\Pi_{3/2})$ and $NO(^2\Pi_{1/2})$ are also in qualitative agreement with the experiments. Quantitative comparison is not possible because of the number of approximations made in the calculations and due to the limited number of the rotational/Λ-doublet channels studied in our experiment. Thus, it appears that the PESs calculated by Katagiri and Kato are capable of reproducing the state-specific product spin-orbit ratios observed experimentally, when averaged over the state-to-state fluctuations. The nonadiabatic transitions responsible for such spin-orbit distributions apparently occur at long range, beyond the transition state, where the splittings between the two attractive surfaces connecting the lowest energy molecular surfaces with the asymptotic $NO(^2\Pi_{1/2}) + O(^3P_2)$ surface, and the other surfaces, which are repulsive, are minimized. According to the calculations, at $E^{\ddagger} \sim 400$ cm^{-1} 7−8 bending levels can be populated at the transition state. All the bending−rotational adiabatic curves, except the lowest two, have potential barriers beyond which nonadiabatic transitions can still take place. This may be particularly true for the $NO(J)$ states monitored in the present experiments, which possess low translational energies. Although the probability of nonadiabatic transitions beyond the transition state is significant, the lowest spin−orbit channel is still favored.

V. Summary

Spatial profiles of recoiling NO products have been used to obtain $O(^3P_j)$ product state distributions fully resolved with respect to the quantum state of the correlated NO product in NO₂ photodissociation at $E^{\ddagger} = 390$, 425, and 1054 cm^{-1}. Some implications to the mechanism of NO₂ photodissociation are summarized below.

The state-specific $O(^3P_j)$ population ratios show significant fluctuations with respect to the quantum state of the correlated $NO(^2\Pi_{\Omega},J,\Lambda)$ fragment. Prominent fluctuations are observed (i) at specific $E^{\ddagger}$ when monitoring different NO rotational states or the two Λ-doublet components of the same rotational level and (ii) when monitoring a specific $NO(\Omega,J,\Lambda)$ state at slightly different $E^{\ddagger}$. Thus, the state-to-state nonadiabatic transitions between surfaces correlating with different $O(^3P_j) + NO(^2\Pi_{\Omega})$ channels fluctuate in the same manner observed previously for the rotational states of NO in the same energy region.

13646 *J. Phys. Chem., Vol. 99, No. 37, 1995*

Sanov et al.

The fluctuations in the fully resolved $O(^3P_j)$ distributions do not appear to decrease with excess energy. However, when averaged over all open NO channels, the dependence of the $O(^3P_j)$ branching ratios on excess energy becomes smoother.[4]

On average, the $O(^3P_j)$ population ratios are much colder than statistical. When summed over all studied NO channels, the $O(^3P_j)$ branching ratios are in quantitative agreement with the earlier results by Miyawaki et al.[4]

The $O(^3P_1):O(^3P_2)$ population ratios correlated with $NO(^2\Pi_{3/2})$ are on avarage larger than those correlated with the ground spin–orbit state, $NO(^2\Pi_{1/2})$. This is in accordance with the calculations of Katagiri and Kato, which show that, while the $NO(^2\Pi_{1/2}) + O(^3P_2)$ channel is correlated with two attractive potentials, the potential curves for all other channels are repulsive.[45]

In conclusion, it appears that the unimolecular reaction of NO_2 proceeds predominantly on the ground electronic surface correlating with $NO + O$ products in their lowest spin–orbit states. Nonadiabatic transitions to surfaces correlating with higher spin–orbit states take place in the exit channel with probabilities that exhibit state-to-state fluctuations. On average the final spin–orbit population ratios are colder than statistical.

References and Notes

(1) (a) Zacharias, H.; Geilhaupt, M; Meier, K.; Welge, K. H. *J. Chem. Phys.* **1981**, *74*, 218. (b) Zacharias, H.; Meier, K.; Welge, K. H. In *Energy Storage and Redistribution in Molecules*; Hinze, J., Ed.; Plenum: New York, 1983; p 107. (c) Robra, U.; Zacharias, H.; Welge, K. H. *Z. Phys. D* **1990**, *16*, 175.

(2) Rubahn, H.-G.; Zande, W. J. van der; Zhang, R.; Bronikowski, M. J.; Zare, R. N. *Chem. Phys. Lett.* **1991**, *186*, 154.

(3) (a) Haller, E.; Köppel, H.; Cederbaum, L. S. *J. Mol. Specrosc.* **1985**, *111*, 377. (b) Köppel, H.; Domcke, W.; Cederbaum, L. S. *Adv. Chem. Phys.* **1984**, *57*, 59.

(4) (a) Miyawaki, J.; Yamanouchi, K.; Tsuchiya, S. *Chem. Phys. Lett.* **1991**, *180*, 287. (b) Miyawaki, J.; Tsuchizawa, T.; Yamanouchi, K.; Tsuchiya, S. *Ibid.* **1990**, *165*, 168.

(5) Miyawaki, J.; Yamanouchi, K.; Tsuchiya, S. *J. Chem. Phys.* **1993**, *99*, 254.

(6) (a) Robie, D. C.; Hunter, M.; Bates, J. L.; Reisler, H. *Chem. Phys. Lett.* **1992** *193*, 413. (b) Hunter, M.; Reid, S. A.; Robie, D. C.; Reisler, H. *J. Chem. Phys.* **1993** *99*, 1093.

(7) (a) Reid, S. A.; Brandon, J. T.; Hunter, M.; Reisler, H. *J. Chem. Phys.* **1993** *99*, 4860. (b) Reid, S. A.; Robie, D. C.; Reisler, H. *Ibid.* **1994** *100*, 4256. (c) Reid, S. A.; Reisler, H. *Ibid.* **1994** *101*, 5683.

(8) (a) Brucker, G. A.; Ionov, S. I.; Chen, Y.; Wittig, C. *Chem. Phys. Lett.* **1992**, *194*, 301. (b) Ionov, S. I.; Brucker, G. A.; Jaques, C.; Chen, Y.; Wittig, C. *J. Chem. Phys.* **1993**, *99*, 3420.

(9) (a) Gaedtke, H.; Troe, J. *Ber. Bunsen-Ges. Phys. Chem.* **1975**, *79*, 184. (b) Quack, M.; Troe, J. *Ibid.* **1975**, *79*, 469. (c) Gaedtke, H.; Hippler, H.; Troe, J. *Chem. Phys. Lett.* **1972**, *16*, 177.

(10) Knepp, P. T.; Terentis, A. C.; Kable, S. H. *J. Chem. Phys.* **1995**, *103*, 194.

(11) Busch, G. E.; Wilson, K. R. *J. Chem. Phys.* **1972**, *56*, 3638.

(12) (a) Mons, M.; Dimicoli, I *Chem. Phys. Lett.* **1986**, *131*, 298. (b) Mons, M.; Dimicoli, I. *J. Chem. Phys.* **1989**, *90*, 4037.

(13) (a) Suzuki, T.; Hradil, V. P.; Hewitt, S. A.; Houston, P. L. *Chem. Phys. Lett.* **1991**, *187*, 257. (b) Hradil, V. P.; Suzuki, T.; Hewitt, S. A.; Houston, P. L.; Whitaker, B. J. *J. Chem. Phys.* **1993**, *99*, 4455.

(14) (a) Butenhoff, T. J.; Rohlfing, E. A. *J. Chem. Phys.* **1993**, *98*, 5460. (a) Butenhoff, T. J.; Rohlfing, E. A. *Ibid.* **1993**, *98*, 5469.

(15) Grünefeld, G.; Andresen, P. *Chem. Phys. Lett.* **1993**, *208*, 369.

(16) McFarlane, J.; Polanyi, J. C.; Shapter, J. G. *J. Photochem. Photobiol. A: Chem.* **1991**, *58*, 139.

(17) Rohlfing, E. A.; Valentini, J. J. *J. Chem. Phys.* **1985**, *83*, 521.

(18) Harrison, J. A.; Yang, X.; Rösslein, M.; Felder, P.; Huber, J. R. *J. Phys. Chem.* **1994**, *98*, 12260.

(19) Changlong, N.; Hua, L.; Pfab, J. *J. Chem. Phys.* **1993**, *97*, 7458.

(20) (a) Delon, A.; Jost, R. *J. Chem. Phys.* **1991**, *95*, 5686. (a) Delon, A.; Jost, R.; Lombardi, M. *Ibid.* **1991**, *95*, 5700.

(21) Hardwick, J. L. *J. Mol. Spectrosc.* **1985**, *109*, 85.

(22) Ionov, S. I.; Davis, H. F.; Mikhaylichenko, K.; Valachovic, L.; Beaudet, R. A.; Wittig, C. *J. Chem. Phys.* **1994** *101*, 4809.

(23) (a) Ericson, T. *Ann. Phys.* **1963**, *23*, 390. (b) Ericson, T. *Phys. Rev. Lett.* **1960**, *5*, 430.

(24) Robinson, P. J.; Holbrook, K. A. *Unimolecular Reactions*; Wiley: London, 1972.

(25) Forst, W. *Theory of Unimolecular Reactions*; Academic: New York, 1973.

(26) (a) Pechukas, P.; Light, J. C.; Rankin, C. *J. Chem. Phys.* **1966**, *44*, 794. (b) Pechukas, P.; Light, J. C. *Ibid.* **1965**, *42*, 3281. (c) Light, J. C. *Discuss. Faraday Soc.* **1967**, *44*, 14.

(27) Klotz, C. E. *J. Phys. Chem.* **1971**, *75*, 1526.

(28) (a) Wardlaw, D. M.; Marcus, R. A. *Chem. Phys. Lett.* **1984**, *110*, 230. (b) *J. Chem. Phys.* **1985**, *83*, 3462. (c) *Adv. Chem. Phys.* **1988**, *70*, 231.

(29) Klippenstein, S. J.; Radivoyevitch, T. *J. Chem. Phys.* **1993**, *99*, 3644.

(30) (a) Peskin, U.; Reisler, H.; Miller, W. H. *J. Chem. Phys.* **1994**, *101*, 9672. (b) Peskin, U.; Miller, W. H.; Reisler, H. *J. Chem. Phys.* **1995**, *102*, 8874.

(31) Reisler, H.; Keller, H.-M.; Schinke, R. *Comments At. Mol. Phys.* **1994**, *30*, 191.

(32) Schinke, R. *Photodissociation Dynamics*; Cambridge University: Cambridge, 1993.

(33) Green, W. H., Jr.; Moore, C. B.; Polik, W. F. *Annu. Rev. Phys. Chem.* **1992**, *43*, 307.

(34) (a) Reisler, H.; Wittig, C. In *Advances in Kinetics and Dynamics*; Barker, J. R., Ed.; JAI Press: Greenwich, 1992; Vol. 1. (b) Reisler, H.; Wittig, C. *Annu. Rev. Phys. Chem.* **1986**, *37*, 307.

(35) (a) Khundkar, L. R.; Knee, J. L.; Zewail, A. H. *J. Chem. Phys.* **1987**, *87*, 77. (b) Klippenstein, S. J.; Khundkar, L. R.; Zewail, A. H.; Marcus, R. A. *Ibid.* **1988**, *89*, 4761.

(36) (a) Qian, C. X. W.; Noble, M.; Nadler, I.; Reisler, H.; Wittig, C. *J. Chem. Phys.* **1985**, *83*, 5573. (b) Wittig, C.; Nadler, I.; Reisler, H.; Noble, M.; Catanzarite, J.; Radhakrishnan, G. *Ibid.* **1985**, *83*, 5581.

(37) Katagiri, H.; Kato, S. *J. Chem. Phys.* **1993**, *99*, 8805.

(38) Hsu, D. K.; Monts, D. L.; Zare, R. N. *Spectral Atlas of Nitrogen Dioxide 5530 to 6480 Å*; Academic: New York, 1978.

(39) Hertz, R. A.; Syage, J. A. *J. Chem. Phys.* **1994**, *100*, 9265.

(40) Kawasaki, M.; Sato, H.; Fukuroda, A.; Kikuchi, T.; Kobayashi, S.; Arikawa, T. *J. Chem. Phys.* **1987**, *86*, 4431.

(41) Zare, R. N. *Mol. Photochem.* **1972**, *4*, 1.

(42) Wiley, W. C.; McLaren, I. H. *Rev. Sci. Instrum.* **1955**, *26*, 1150.

(43) Miller, J. C.; Compton, R. N. *Chem. Phys.* **1981**, *75*, 22.

(44) Jacobs, D. C.; Zare, R. N. *J. Chem. Phys.* **1986**, *85*, 5457.

(45) Graff, M. M.; Wagner, A. F. *J. Chem. Phys.* **1990**, *92*, 2423.